Supporting Information

Activating Titania for Efficient Electrocatalysis by Vacancy Engineering

Haifeng Feng,[†,§,⊥] Zhongfei Xu,[‡,§,⊥] Long Ren,[†,⊥] Chen Liu,[∥] Jincheng Zhuang,[†] Zhenpeng Hu,[#,*] Xun Xu,[†,§] Jun Chen,[▽] Jiaou Wang,[∥] Weichang Hao,[‡,§,*] Yi Du,[†,§,*] and Shi Xue Dou,[†,§]

[†]Institute for Superconducting and Electronic Materials, Australian Institute for Innovative Materials, University of Wollongong, Wollongong, NSW 2500, Australia

[‡]Department of Physics and Key Laboratory of Micro-Nano Measurement, Manipulation and Physics, Ministry of Education, Beihang University, Beijing 100191, P. R. China

[§]Beihang-UOW Joint Research Centre, Beihang University, Beijing 100191, P. R. China

[∥]Beijing Synchrotron Radiation Facility, Institute of High Energy Physics, Chinese Academy of Sciences, Beijing 100049, P. R. China

[#]School of Physics, Nankai University, Tianjin 300071, P. R. China

[▽]Intelligent Polymer Research Institute and ARC Centre of Excellence for Electromaterials Science, University of Wollongong, Wollongong, NSW 2500, Australia

Corresponding Author

* yi_du@uow.edu.au

* whao@buaa.edu.cn

* zphu@nankai.edu.cn

Materials and Methods

Rutile TiO_2(110) single crystal (5 × 5 × 1 mm) was purchased from Mateck, GmbH. To obtain the reduced TiO_2, the rutile single crystals were annealed in ultra-high vacuum (UHV) at 900 K. The samples with a high concentration and a low concentration of oxygen vacancies (OVs) were annealed for around

50 h and 5 h, respectively. Scanning tunneling microscope (STM) images were acquired by using a low-temperature scanning tunneling microscope (LT-STM) (USM 1500-M, Unisoku Co.) at 78 K, in constant current mode. The samples in STM measurements were treated by several cycles of Ar^+ sputtering (1 kV, 20 min) and annealing (900 K, 1 h). The cross-sectional TEM images were acquired with a scanning transmission electron microscope (STEM, JEOL JEM-ARM200f) both in high angle annular dark field (HAADF) mode and annular bright field (ABF) mode. In-situ electron energy loss spectroscopy (EELS) was used to characterize the OV concentration of the cross-sectional sample in TEM measurements. The cross-sectional sample was prepared by the focused ion beam (FIB, Zeiss Auriga FIB-SEM) technique.

In-situ X-ray photoelectron spectroscopy (XPS) characterizations were carried out at Beamline 4B9B in the Beijing Synchrotron Radiation Facility (BSRF), and variable photon energies were referenced to a fresh Au polycrystalline film. The spot size of incident light in XPS was about 1 mm in diameter. All the data were recorded in UHV at room temperature. The Hall coefficient and magnetoresistance were measured by the five-probe technique using a Quantum Design Physical Property Measurement System (PPMS)-14T. The electrolyte was 1 M KOH solution. The electrochemical HER experiments were performed by a typical three-electrode method, in which a Pt plate and Hg/HgO (0.923 V versus the standard hydrogen electrode) were used as the counter and reference electrodes, respectively. All electrochemical measurements were performed with a Bio Logic Science Instruments VSP-300 electrochemistry workstation. The linear portions of Tafel plots were fitted to the Tafel equation: $\eta = b\log|J| + a$, where η is the overpotential, a is the exchange current density, and b is the Tafel slope.

All density functional theory (DFT) calculations were performed using the Vienna Ab Initio Simulation Package (VASP). The generalized gradient approximation (GGA) was applied to treat the exchange correlation energy with the Perdew−Burke−Ernzerhof (PBE) functional. The projector augmented wave (PAW) method was employed to describe electron−ion interactions, with the cut-off energy of 400 eV. The structural model of the TiO_2(110) surface was constructed with four Ti-O layers as a 4 × 2 periodic supercell comprising 192 atoms with a vacuum spacing of 20 Å to avoid interaction between adjacent surfaces. Spin-polarized local density approximation plus on-site Coulomb self-interaction potential (LDA+U) calculations were performed for the Hubbard correction, and an effective U (U_{eff}) value of 4.2 eV was applied in all calculations. All structures in the calculations were relaxed until the convergence tolerance of the force on each atom was smaller than 0.02 eV. The energy convergence criterion was set

to be 1×10^{-4} eV for self-consistent calculations, and *k*-point sampling was restricted to the Gamma point only because of the large size of the supercell.

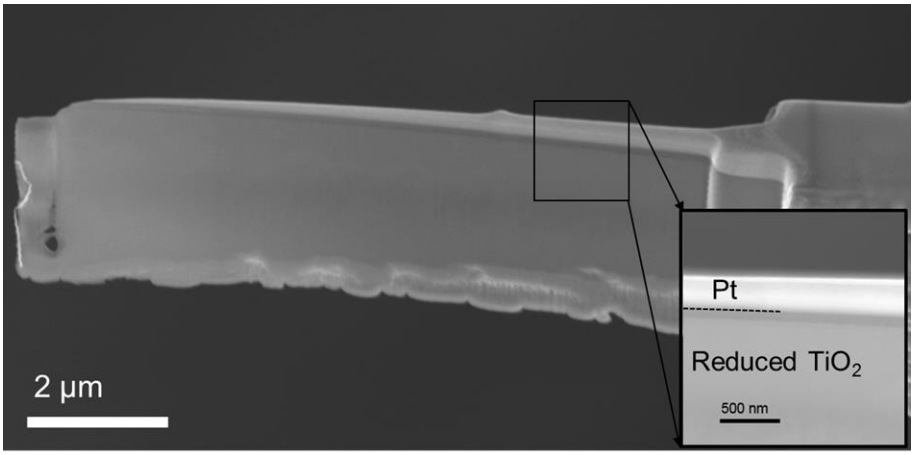

Figure S1. SEM image of reduced TiO_2 single crystal sample cut by a focused ion beam (FIB); inset is an enlarged image of the selected area.

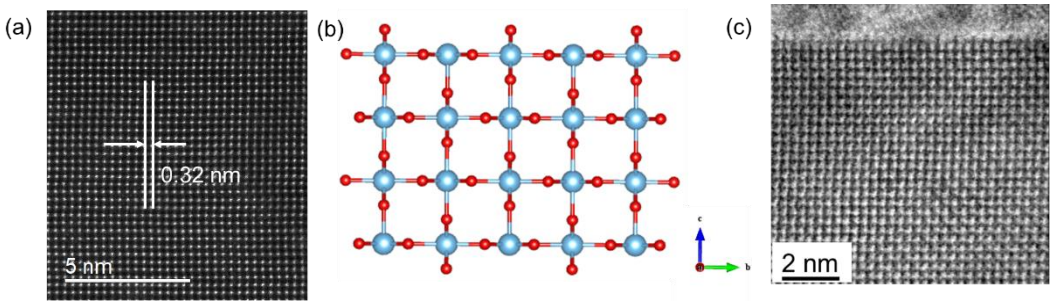

Figure S2. STEM image of the cross section of the reduced TiO_2 single crystal and its crystal structure diagram. (a) STEM image of the projection face of the FIB cut cross-sectional sample, with the Ti atoms appearing as bright spots. (b) Schematic diagram of the crystal structure of the projection face in (a), with the top surface the (110) surface. The red balls represent oxygen atoms, and the blue balls represent Ti atoms. (c) Cross-sectional STEM image of the reduced TiO_2 single crystal in annular bright field (ABF) mode.

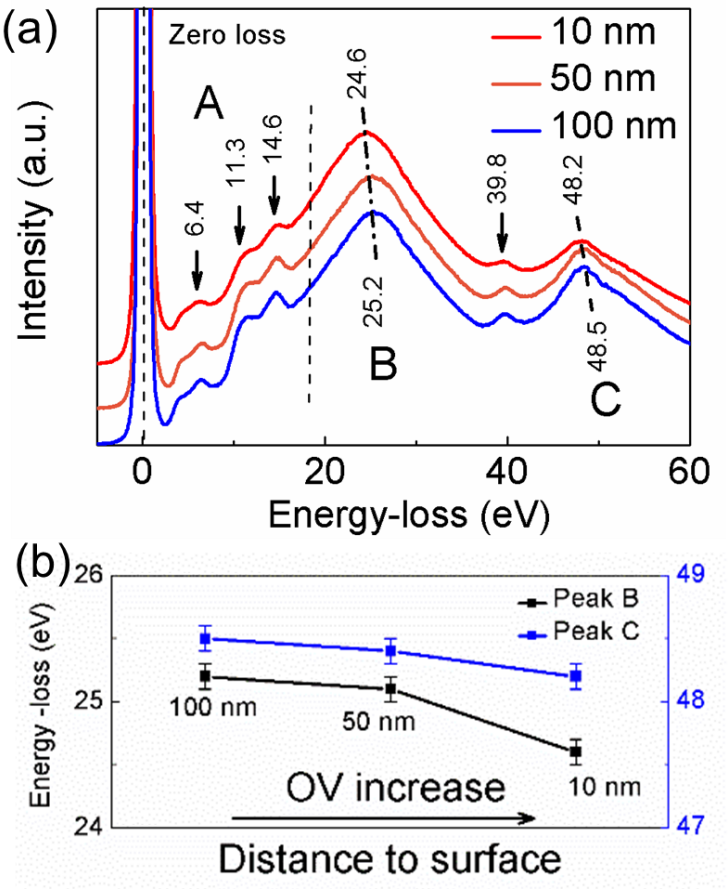

Figure S3. In-situ low-level EELS spectra of the reduced TiO_2 single crystal. (a) *In-situ* EELS low-level spectra of the regions marked in Fig. 1b. Three peaks in region A, which exhibited obvious broadening are indicated by black arrows. (b) The shifts of peaks B and C in (a), indicating the changing trends in the OV concentration from the inner region to the surface of the reduced TiO_2 single crystal.

As shown in Fig. S3, the three peaks (6.4 eV, 11.3 eV, and 14.6 eV), originating from O 2*p* orbitals to Ti 3*d* orbitals, are marked in region A. Compared with the inner region, the peaks from the surface region (10 nm) exhibited obvious broadening, which was caused by the OV induced lattice distortion and indicated a higher OV concentration near the top surface area.[1] Meanwhile, the peaks at 25.2 eV (peak B) and 48.5 eV (peak C) in the inner region shifted towards lower energy, to 24.6 eV and 48.2 eV, in the top surface region, due to the emergence of more OVs. Peak B was assigned to electron transitions between the O 2*p* state and Ti 4*sp* states. Peak C was assigned to electron excitations from the Ti 3*p* core level to 3*d* excited states.[2] Therefore, the presence of OVs is expected to modify the valence states of their surrounding Ti atoms.

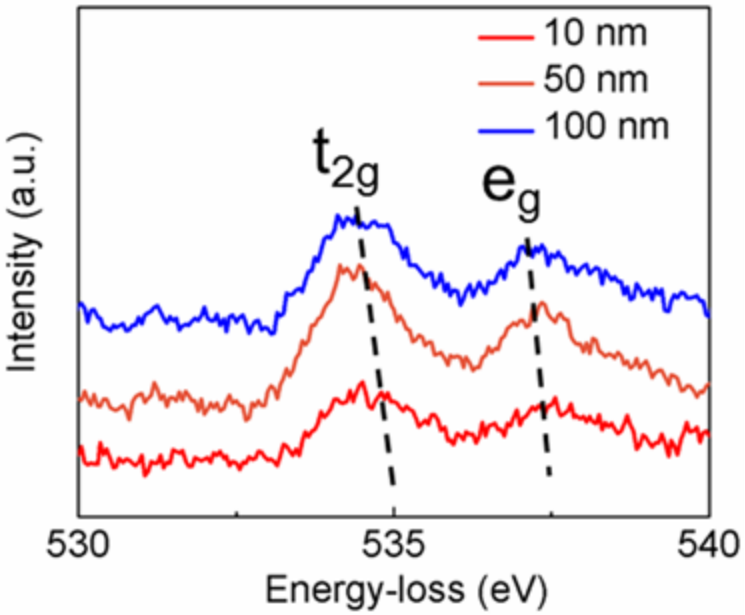

Figure S4. O-*K* edge EELS spectra of the of the regions marked in Fig. 1b. The O-*K* spectra were systematically shifted to higher energy losses with decreasing valence state of Ti, which agrees well with the increasing OV concentration near the surface region.

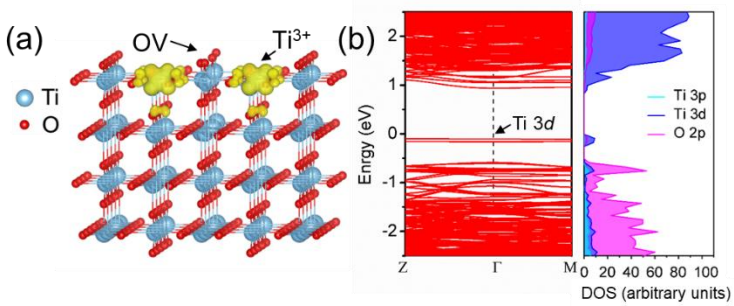

Figure S5. DFT calculations of the mid-gap states caused by OVs in TiO_2(110). (a) Calculation of the excess electron distribution of the reduced TiO_2(110) surface with an OV on the top surface. (b) The calculated band structure (left) and DOS (right) of the TiO_2(110) with a surface OV.

Density functional theory (DFT) calculations were used to verify the OV-induced changes in the electronic structure of the reduced TiO_2. As shown in Fig. S5a and 5b, after introducing an OV on the surface of TiO_2(110), the two excess electrons that belonged to the removed oxygen atom will bond with two neighboring Ti atoms and form Ti^{3+} ions. As a consequence, defect states in the gap, located at around 1 eV below the conduction band (CB), can be observed in the calculated band structure and den-

sity of states (DOS), which are mainly attributed to the Ti 3*d* orbitals. The DFT results indicate that the mid-gap Ti 3*d* defect states originate from OVs and associated Ti^{3+} ions in the reduced TiO_2.

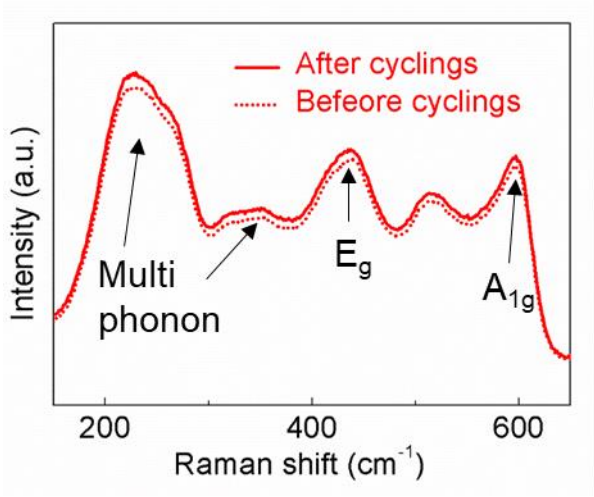

Figure S6. Raman spectra of the reduced TiO_2 single crystal, showing no changes before and after 1000 cycles in the HER test.

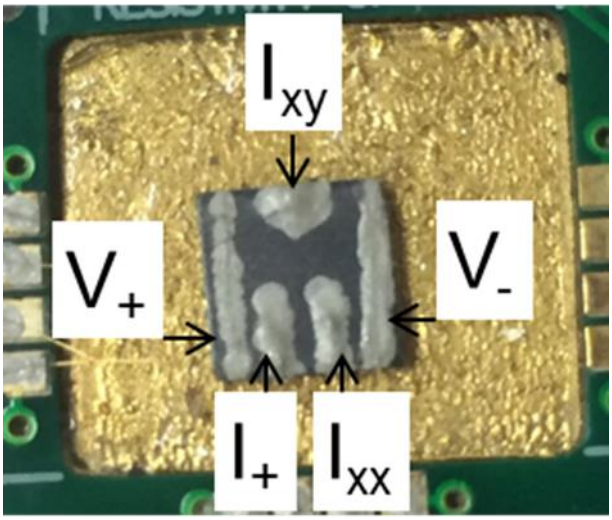

Figure S7. The holder used in PPMS measurement and the five probes configuration used in the PPMS measurement.

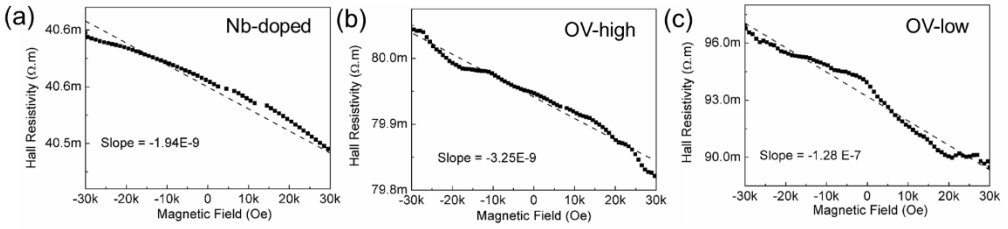

Figure S8. Hall resistivity measurements of different samples. The Hall coefficient R_H was determined by fitting the slope of the curve of the Hall resistivity vs. magnetic field. (a) the Hall resistivity *vs.* magnetic field of Nb-doped TiO_2. (b) the Hall resistivity *vs.* magnetic field of OV-high TiO_2. (c) the Hall resistivity *vs.* magnetic field of OV-low TiO_2.

The electron density of *n*-type semiconductors has an inversely proportional relationship with the Hall coefficient (R_H) as $n = -1/(e \cdot R_H)$, which is consistent with the experimental result that OVs are the dominant defects. Therefore, the electron density of Nb-doped TiO_2, OV-high TiO_2 and OV-low TiO_2 was determined to be 3.2×10^{17} cm^{-3}, 1.9×10^{17} cm^{-3}, and 4.8×10^{15} cm^{-3}, respectively.

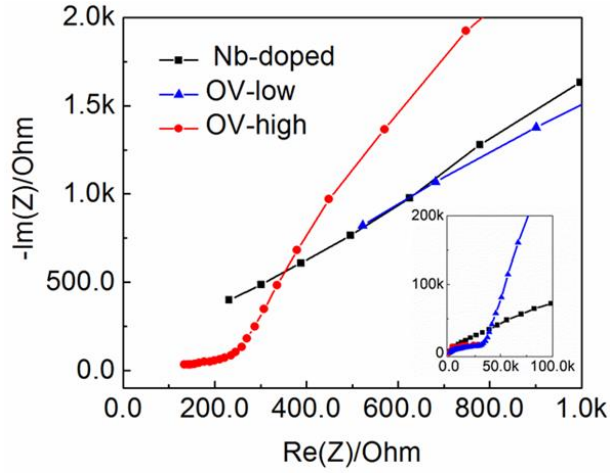

Figure S9. Electrochemical impedance spectra of different electrodes at −0.3 V versus RHE (inset is the full range measurement).

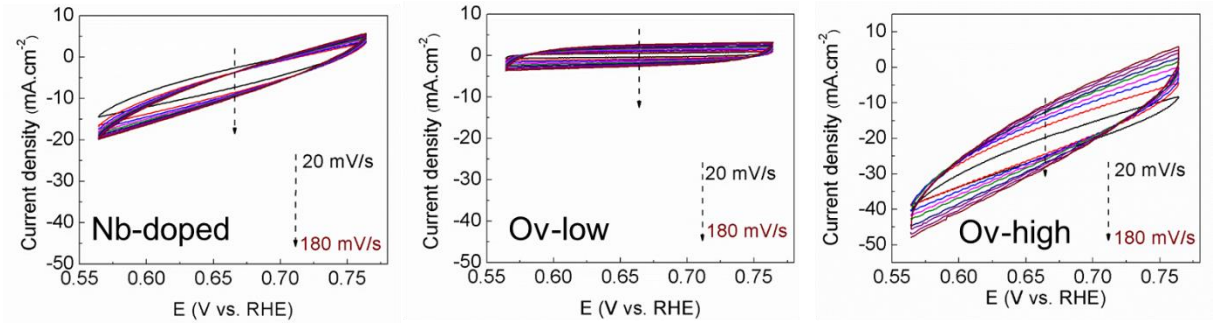

Figure S10. Cyclic voltammetry (CV) curves of different samples.

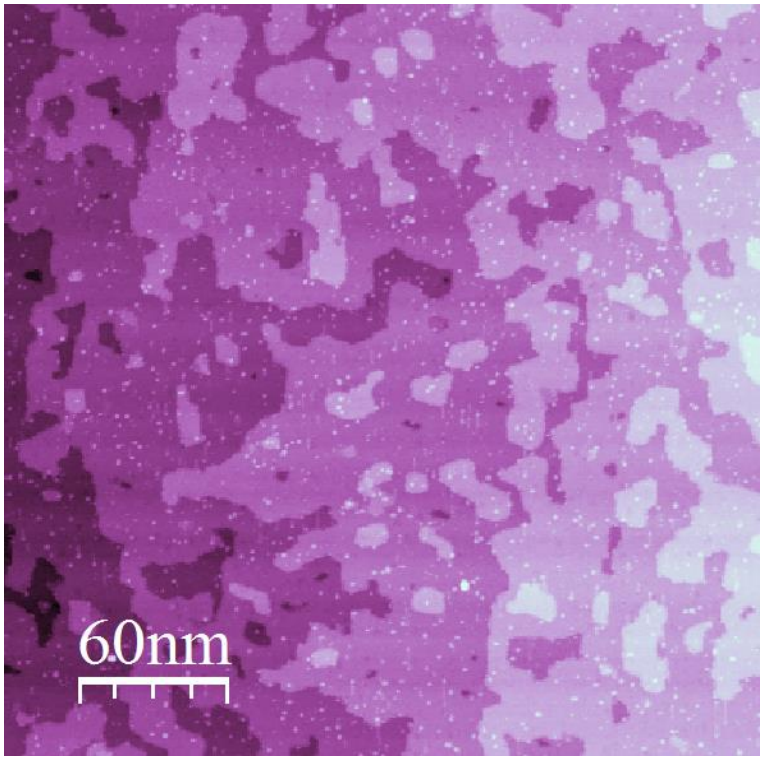

Figure S11. Large scale STM image of the reduced TiO_2 surface (1.3 V, 30 pA).

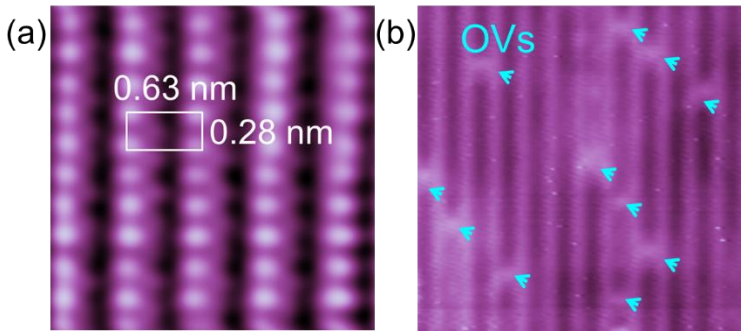

Figure S12. Surface atomic structure of stoichiometric TiO_2 single crystal and TiO_2 single crystal with OVs. (a) Atomic resolution STM image of stoichiometric TiO_2 surface (0.8 V, 200 pA). (b) The reduced TiO_2 surface with OVs on the surface (1.2 V, 20 pA).

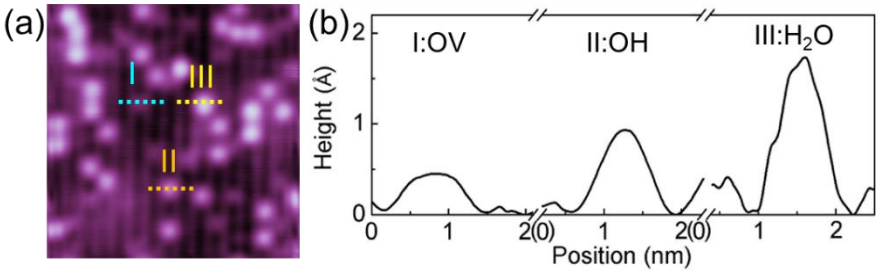

Figure S13. Apparent heights of OV, OH group and H_2O in STM images. (a) STM image of the surface of TiO_2(110) (10 nm × 10 nm, 1.6 V, 30 pA). OV, OH, and H_2O are bright protrusions between two adjacent Ti rows. (b) Line profiles of the defects in (a).

Fig. S12 shows a typical empty-state STM image of the surface structure of the reduced TiO_2, which agrees well with the 1×1 structure model in Fig. 1a. Since the empty-state of TiO_2 is dominated by the Ti-3*d* electronic states, Ti_{5C} atoms and O_{br} atoms appear as bright and dark rows in the empty-state STM image, respectively, which is reverse-contrast of their real topographies.[3] According to previous studies, the majority defects on this reduced TiO_2 surface are OVs, which appear as bright protrusions between two adjacent Ti_{5C} rows (cantered on dark oxygen rows). Because OVs are very reactive towards adsorbing and dissociating residual water molecules on the surface, OH groups (formed by the dissociation of water molecules at OV sites) and non-dissociated water molecules (adsorbed at OV sites) can also be observed as bright protrusions in the empty-state STM images. These three types of bright protrusions (marked as I, II, and III) exhibit different brightness and apparent heights (indicated in Fig. S13), which can be used not only in identifying different species, but also in monitoring their dynamic reaction processes.[4-7]

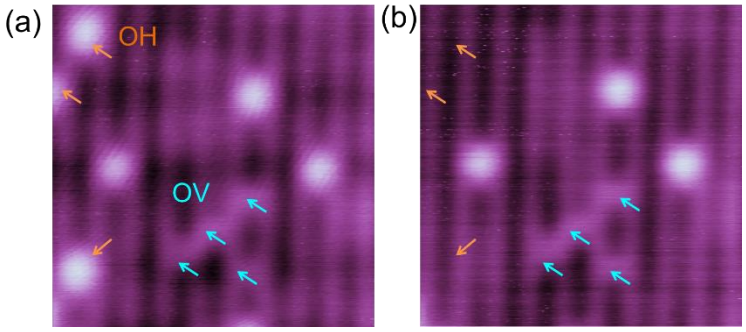

Figure S14. (a) STM image of the reduced rutile TiO_2(110) surface with OVs and OHs (1.3 V, 30 pA). (b) STM image in a same area in (a), in which 2.5 V pulses were applied at the marked OHs (1.3 V, 30 pA).

As discussed in Fig. S13, OH, OV, and H_2O can be identified through measuring their apparent height in the empty-state STM images. They can also be identified by applying a voltage higher than a threshold voltage (around 2.0 V in our measurements), either through giving pulses or scanning. As shown in Fig. S14, when three 2.5 V pulses were applied at the selected OHs marked in Fig. S14a, the hydrogen atoms were removed, allowing the OV to be healed. In the case of OVs, they are always inactive towards 2.5 V pulses or scanning. Therefore, by a combination of their apparent heights and their different behavior under a bias higher the threshold voltage, we can identify them. This phenomenon has been reported in previous works.[4,5]

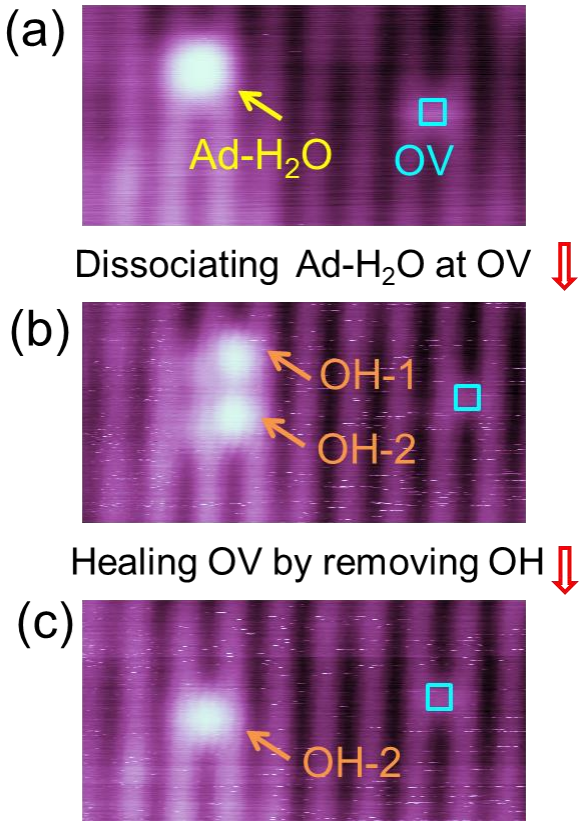

Figure S15. (a) STM image of an individual Ad-H_2O at an OV site, with another OV included as a reference point (3 nm × 6 nm, 1.2 V, 10 pA). (b) STM image of the two OHs from the dissociation of Ad-H_2O at the OV site (1.2 V, 10 pA). (c) STM image of the same area in a and b, in which an OH was removed through a 2.5 V pulse by the STM tip (1.2 V, 10 pA).

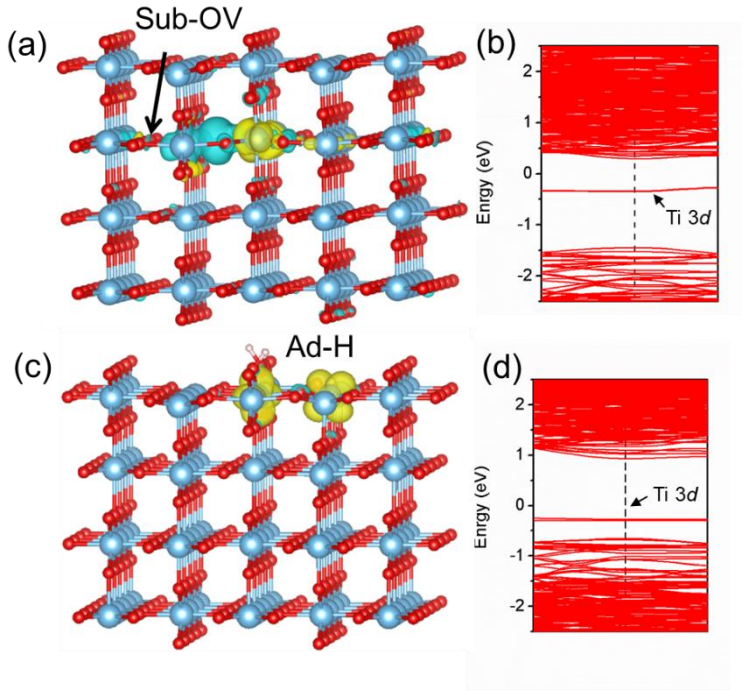

Figure S16. Calculation of the excess electron distribution on the TiO_2(110) surface with a OV on the sublayer and with two surface Ad-H. (a) and (b) The calculated band structure and DOS of TiO_2(110) with sublayer OVs, respectively. (c) and (d) The calculated band structure and DOS of TiO_2(110) with surface Ad-Hs, respectively.

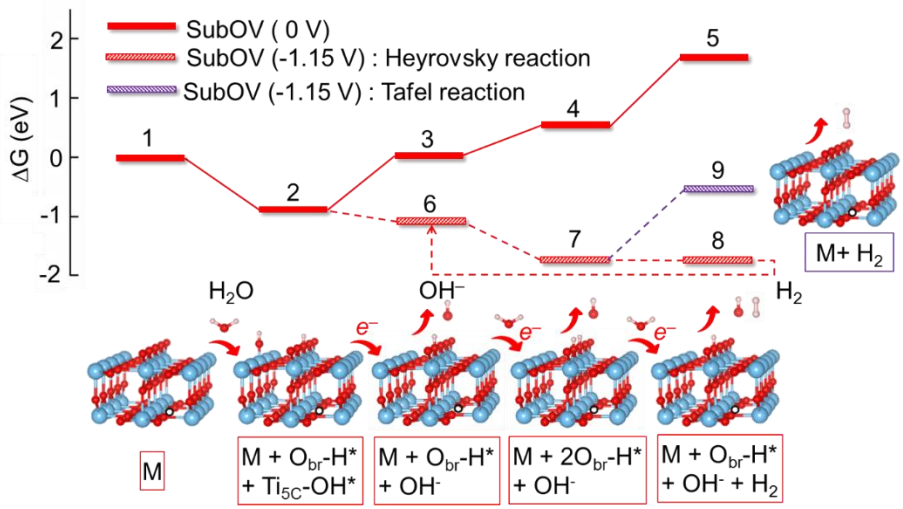

Figure S17. Optimized pathway of the HER in alkaline media on the reduced TiO_2 with subOV based on the free energy calculation.

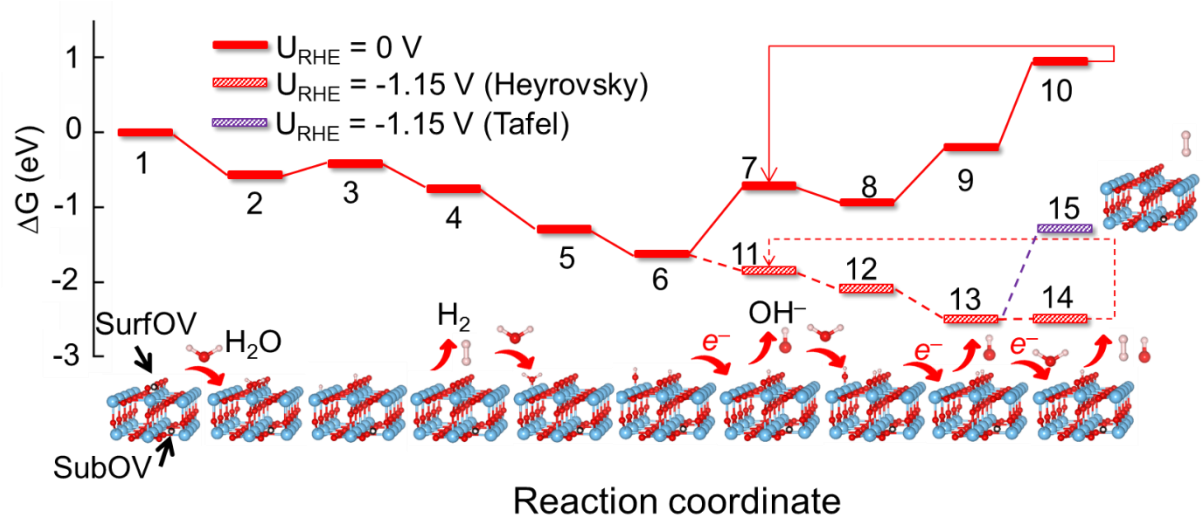

Figure S18. Optimized pathway of the HER in alkaline media on the reduced TiO_2 with surfOv and subOV based on the free energy calculation.

Intermediates 1: TiO_2-surfOV-subOV + H_2O TiO_2-subOV + surfOV-H_2O*

2: TiO_2-subOV + surfOV-H_2O*

3: TiO_2-subOV + O_{br}-H* + Ti-H*

4: TiO_2-subOV + H_2

5: TiO_2-subOV + Ti_{5C}-H_2O*

6: TiO_2-subOV + Ti_{5C}-OH* + O_{br}-H*

7 and 11: TiO_2-subOV + O_{br}-H* + OH^-

8 and 12: TiO_2-subOV + 2O_{br}-H* + Ti_{5C}-OH*

9 and 13: TiO_2-subOV + 2O_{br}-H* + OH^-

10 and 14: TiO_2-subOV + O_{br}-H* + OH^- + H_2

15: TiO_2-subOV + H_2

All reactions are written as:

a. TiO_2-surfOV-subOV:

Volmer (1-2-3)

TiO_2-surfOV-subOV + H_2O → TiO_2-subOV + surfOV-H_2O^*

TiO_2-subOV + surfOV-H_2O^* → TiO_2-subOV + O_{br}-H^* + Ti_{5C}-H^*

Tafel (3-4)

TiO_2-subOV + O_{br}-H^* + Ti_{5C}-H^*→ TiO_2-subOV + H_2↑

b. TiO_2-subOV:

Volmer (4-5-6)

TiO_2-subOV+ $H_2O \rightarrow TiO_2$-subOV + Ti_{5C}-H_2O^*

TiO_2-subOV + Ti_{5C}-$H_2O^* \rightarrow TiO_2$-subOV + Ti_{5C}-OH^* + O_{br}-H^*

Heyrovsky (6-11)

TiO_2-subOV + Ti_{5C}-OH^* + O_{br}-$H^* \rightarrow TiO_2$-subOV + O_{br}-H^* + ($OH^- - e^-$)

c. TiO_2-subOV + O_{br}-H^*:

Volmer (11-12-13)

TiO_2-subOV + O_{br}-H^* +$H_2O \rightarrow TiO_2$-subOV + 2O_{br}-H^* + Ti_{5C}-OH^*

TiO_2-subOV + 2O_{br}-H^* + Ti_{5C}-$OH^* \rightarrow TiO_2$-subOV + 2O_{br}-H^* + ($OH^- - e^-$)

Heyrovsky (13-14)

TiO_2-subOV + 2O_{br}-H^* + $H_2O \rightarrow TiO_2$-subOV + O_{br}-H^* + $H_2\uparrow$ + ($OH^- - e^-$)

Tafel (13-15)

TiO_2-subOV + 2O_{br}-$H^* \rightarrow TiO_2$-subOV + $H_2\uparrow$

The calculation methods for the hydrogen evolution reaction (HER) in alkaline solutions are summarized as follows:

1. By considering the standard hydrogen electrode as the reference potential and hydrolysis of water in the solution, the free energy of reactions (1) and (2) is set to zero because they are in equilibrium. Therefore, the free energy of ($H^+ + e^-$) corresponds to that of ½ H_2 (1 bar, 298 K) and the free energy of ($OH^- - e^-$) is calculated according to the free energy of H_2O and ($H^+ + e^-$),

$$(H^+ + e^-) \rightarrow ½\ H_2 \quad (1)$$

$$H_2O \rightarrow (H^+ + e^-) + (OH^- - e^-) \quad (2)$$

We used gas-phase H_2O at 0.035 bar as the reference state, because at this pressure, gas-phase H_2O is in equilibrium with liquid water at 300 K. The calculated free energies of the H_2O, ($H^+ + e^-$), and ($OH^- - e^-$) are listed in Supplementary Table S1.

2. The Gibbs free energy of the intermediates were calculated as[8]

$$\Delta G = \Delta E + \Delta ZPE - T\Delta S \quad (3)$$

where ΔE is the binding energy of intermediates which is defined as the reaction energies of the reactions

$$H_2O + * \rightarrow OH^* + H^* \quad (4)$$

$$H_2O + * \rightarrow OH^* + \tfrac{1}{2}H_2 \quad (5)$$

$$\tfrac{1}{2}H_2 + * \rightarrow H^* \quad (6)$$

ΔZPE and ΔS can be obtained from the vibrational frequency υ_i, which are the changes in zero point energies and entropies due to the reaction, respectively. All the parameters have been taken from DFT calculations.

Zero point energies are calculated as follows,

$$ZPE = \sum_i \tfrac{1}{2} h\upsilon_i \quad (7)$$

i = 3*n*–5 (for linear molecule)

i = 3*n*–6 (for non-linear molecule)

where *i* is the degree of freedom for the molecule, and *n* is the number of atoms in the molecule.

Entropies are calculated from the sum of the translational entropy S_t, the rotational entropy S_r, and the vibrational entropy S_v as follows:

$$S = S_t + S_r + S_v \quad (8)$$

$$S_t = Nk_B \left\{ \ln \left[\frac{(2\pi m k_B T)^{\frac{3}{2}}}{N_A h^3} \cdot \frac{V}{N} \right] + \frac{5}{2} \right\} \quad (9)$$

$$S_r = Nk_B \left(\ln \frac{8\pi^2 I k_B T}{\sigma h^2} + 1 \right) \text{ (for linear molecule) (10-1)}$$

$$S_r = Nk_B \left[\ln \frac{8\pi^2 (2\pi k_B T)^{\frac{3}{2}}}{\sigma h^3} \cdot (I_x I_y I_z)^{\frac{1}{2}} + 1 \right] \text{ (for non-linear molecule) (10-2)}$$

$$S_v = \sum_i Nk_B \left[\frac{h\nu_i / k_B T}{e^{h\nu_i / k_B T} - 1} - \ln\left(1 - e^{-h\nu_i / k_B T}\right) \right] \quad (11)$$

Where k_B, N_A, and *h* are the Boltzmann constant, Avogadro constant, and Planck constant, respectively. N, *m*, *V*, *T*, *I*, and σ are the number of particles, and the mass, volume, temperature, moment of inertia, and symmetry number of the molecules, respectively. Otherwise, the entropies of intermediates are calculated by the vibrational entropy S_v, because no translational or rotational behaviors can be found for an adsorbed molecule. The calculated *ZPE* and *S* of free H_2O, H_2, and (OH^- - e^-) are listed in Table S1.

3. At a pH different from 0, we can correct the free energy of H^+ ions by the concentration dependence of the entropy: $\Delta G_{pH} = -kT \cdot \ln[H^+] = kT \cdot \ln 10 \cdot pH$. In our work, pH is 14 and ΔG_{pH} = 0.83 eV.

4. The effect of a bias ΔG_U was imposed on each step by including an electron in the electrode as an –e*U* term, where *U* is the electrode potential relative to the standard hydrogen electrode. Therefore, the reaction free energy of processes was calculated as:

$$\Delta G_{(U, pH)} = \Delta G + \Delta G_{pH} + \Delta G_U \quad (12)$$

As is shown in the reactions of the HER in alkaline solution,

Volmer $H_2O + e^- \rightarrow H^* + OH^-$ (13)

Heyrovsky $H_2O + e^- + H^* \rightarrow H_2 + OH^-$ (14)

Tafel $2H^* \rightarrow H_2$ (15)

We include the effects of pH and U on steps involving (OH^- - e^-). The free energies of possible steps (such as water splitting, hydroxide adsorption, hydroxide desorption, and hydrogen production) were calculated and compared to find out the most optimal path in our calculation. As a result, the reactions in HER and corresponding free energies under applied potential *U* and pH can be written as:

Volmer 1 - water splitting

$$H_2O + M \rightarrow H^* + OH^*$$

$$\Delta G_1 = \Delta G\,(H^* + OH^*)$$

Volmer 2 - OH^* desorption

$$OH^* \rightarrow (OH^- - e^-) + M$$

$$\Delta G_2 = -\Delta G(OH^*) + eU + 0.83$$

Heyrovsky

$$H_2O + H^* \rightarrow H_2\uparrow + (OH^- - e^-) + M$$

$$\Delta G_3 = -\Delta G(H^*) + eU + 0.83$$

Tafel

$$2H^* + M \rightarrow H_2\uparrow$$

$$\Delta G_4 = -\Delta G(2H^*)$$

Here, M represents the catalyst, which can be a TiO_2(110) surface with surfOV and subOV, only subOV, or subOV with O_{br}-H surface. The calculation results of main reaction pathway are listed in Table S1.

Table S1. Binding energies, entropies, and zero point energies contribution to Gibbs free energy of main reaction pathway. subOV + O_{br}-H* is regard as M.

subOV + O_{br}-H^*	ΔE	*ZPE*	ΔZPE	*TS*	$T\Delta S$	ΔZPE-$T\Delta S$	ΔG	ΔG *(pH)*
H_2O		0.566	0	0.534	0	0	0	0
½ H_2		0.133		0.201				
$OH^- - e^-$		0.433		0.333				
H_2O^*	-0.932	0.631	0.065	0.020	-0.514	0.579	-0.353	-0.353
$H^* + OH^*$	-0.735	0.538	-0.028	0.009	-0.525	0.497	-0.238	-0.238
$H^* + (OH^- - e^-)$	-0.600	0.671	0.105	0.333	-0.201	0.306	-0.294	0.536
$½H_2 + (OH^- - e^-)$		0.566	0	0.534	0	0	0	0.83

References

(1) Mohamed, M. H.; Sadeghi, H. R.; Henrich, V. E. Electron-energy-loss Study of the TiO_2(110) Surface. *Phys. Rev. B* **1988**, *37*, 8417–8423.

(2) Fuentes, G. G.; Mancheño, I. G.; Balbás, F.; Quirós, C.; Trigo, J. F.; Yubero, F.; Elizalde, E.; Sanz, J. M. Dielectric Properties of Ti, TiO_2 and TiN from 1.5 to 60 eV Determined by Reflection Electron Energy Loss Spectroscopy (REELS) and Ellipsometry. *Phys. Stat. Sol. (a)* **1999**, *175*, 429–436.

(3) Diebold U. The Surface Science of Titanium Dioxide. *Surf. Sci. Rep.* **2003**, *48*, 53−229.

(4) Bikondoa, O.; Pang, C. L.; Ithnin, R.; Muryn, C. A.; Onishi, H.; Thornton, G. Direct Visualization of Defect-mediated Dissociation of Water on TiO_2(110). *Nat. Mater.* **2006**, *5*, 189–192.

(5) Cui, X.; Wang, Z.; Tan, S.; Wang, B.; Yang, J.; Hou, J. G. Identifying Hydroxyls on the TiO_2(110)-1×1 Surface with Scanning Tunneling Microscopy. *J. Phys. Chem. C* **2009**, *113*, 13204–13208.

(6) Petrik, N. G.; Zhang, Z.; Du, Y.; Dohnálek, Z.; Lyubinetsky, I.; Kimmel. G. A. Chemical Reactivity of Reduced TiO_2(110): The Dominant Role of Surface Defects in Oxygen Chemisorption. *J. Phys. Chem. C* **2009**, *113*, 12407–12411.

(7) Wendt, S.; Schaub, R.; Matthiesen, J.; Vestergaard, E. K.; Wahlström, E.; Rasmussen, M. D.; Thostrup, P.; Molina, L. M.; Lægsgaard, E.; Stensgaard, I.; Hammer, B.; Besenbacher, F. Oxygen Vacancies on TiO_2(110) and Their Interaction with H_2O and O_2: A Combined High-resolution STM and DFT Study. *Surf. Sci.* **2005**, *598*, 226–245.

(8) Nørskov, J. K.; Rossmeisl, J.; Logadottir, A.; Lindqvist, L. Origin of the Overpotential for Oxygen Reduction at A Fuel-Cell Cathode. *J. Phys. Chem. B* **2004**, *108*, 17886–17892.